Structured Input-Output Analysis of Turbulent Flows over Riblets

Talha Mushtaq*
University of Minnesota, Minneapolis, MN 55455, USA

Mitul Luhar†
University of Southern California, Los Angeles, CA 90089, USA

Maziar S. Hemati‡
University of Minnesota, Minneapolis, MN 55455, USA

This paper applies structured input-output (I/O) methods to analyze turbulent channel flows over riblets. Structured I/O provides a reduced-complexity framework for accounting for the nonlinear terms in the Navier-Stokes equations, thus providing a greater degree of fidelity in the analysis of nonlinear flows than the related linear I/O and resolvent-based analysis techniques. We show that structured I/O is capable of predicting I/O gains relevant to the nonlinear flow physics as well as the associated modes that reveal the underlying instability mechanisms driving turbulent flows over riblets. Particularly, we show that the structured I/O analysis highlights dominant instabilities associated with the lift-up mechanism, Tollmien-Schlichting waves, and Kelvin-Helmholtz-type vortices for the turbulent channel flow model. The associated wavenumbers identified for these instabilities are physically consistent with the results found in prior DNS studies. Furthermore, we show that the rectangular and triangular riblets analyzed in this study minimize the I/O gains of the near-wall cycle, leading to the emergence of new smaller-scale structures that have been highlighted in previous DNS studies. Results and findings are reported and discussed for turbulent channel flows at $Re_\tau = 180$ with smooth-walls and both rectangular and triangular riblet patterning.

I. Introduction

Riblet-based flow control is a promising means of reducing drag in turbulent flows. Riblet-based flow control is particularly attractive because it is completely passive and requires no energy expenditure. Several experimental studies and flight tests have shown that riblets can provide drag reduction of up to 8%, which is a promising number [1]. However, not all riblet patterns reduce drag and designing an optimal riblet shape is difficult. The design process typically requires large parametric sweeps over multiple design parameters in experiments or numerical simulations. Such parameter sweeps are expensive in terms of time and resources.

In contrast, input-output (I/O) methods reduce the complexity of the design process by focusing on the input-output behavior of a system. Specifically, these methods do not require extensive simulations to get initial estimates of worst-case perturbations and propagating mechanisms that would potentially induce instability in a fluid system. Thus, I/O methods make an effective intermediary tool to choose the "best" parameters and initial conditions for direct numerical simulations (DNS), which is contrary to tediously performing several DNS runs using random parameters and initial conditions. Hence, the I/O methods have been used extensively to analyze riblet-based and smooth-wall flows in recent years [2–11].

A popular technique that provides a good balance between computational expediency and complexity is the resolvent-based approach. The efficacy of the resolvent framework is shown in various active and passive flow control studies through its use as a tool for synthesizing controllers and optimizing riblet shapes that reduce frictional drag in turbulent channel flows [3, 12, 13]. Particularly, the authors in [3, 13] show that the resolvent framework can determine optimal riblet geometries which minimize high gains induced by the near-wall (NW) modes. Additionally, they showed that the framework can also identify Kelvin-Helmholtz (KH) vortices over rectangular riblets for the same length-scales

---

*Graduate Student, Aerospace Engineering and Mechanics

†Associate Professor, Aerospace and Mechanical Engineering, AIAA Associate Fellow.

‡Associate Professor, Aerospace Engineering and Mechanics, AIAA Associate Fellow

as identified in prior DNS work [14]. Resolvent analysis is also useful in obtaining rank-1 approximations of NSE, which could provide useful insights into the dominant structures that amplify disturbances [3].

Despite its successes, resolvent-based methods have an inherent drawback: resolvent-based methods do not exploit the structure of the quadratic nonlinearity in the incompressible NSE, and so the inputs and outputs considered in the analysis are not necessarily consistent with the structure of the nonlinear terms in the NSE. Although this lack of imposed structure greatly reduces the complexity of the resolvent analysis framework, it also introduces conservatism in I/O gain estimates, which can diminish the apparent importance of key disturbance mechanisms. Certainly, when perturbations are infinitesimally small in a fluid system, linear I/O methods can be used, since nonlinear effects become negligible. However, when perturbations become large, the nonlinear interactions become more relevant and linear approximations fail to capture the dynamics faithfully. Several efforts have been made to address this issue in recent years, including through the use of quadratic constraints [15–19] and structured I/O methods [20–23]. Structured I/O methods in particular offer an attractive reduced-complexity analysis framework, and will be the subject of the current investigation for analyzing turbulent flows over riblets.

The structured I/O framework closely relates to the resolvent framework in the sense that both methods model the quadratic nonlinearity in the incompressible Navier-Stokes (NSE) as a feedback forcing that generates velocity and pressure responses. However, contrary to the structured I/O method, the resolvent framework does not exploit the structure of the quadratic nonlinearity modeled by the feedback forcing, i.e., the forcing term relates to the outputs that feed-through an unstructured approximation of the nonlinearity, which yields highly conservative estimates of I/O gains and modes. Specifically, structured I/O methods compute I/O gains and mode shapes of a linear time-invariant (LTI) system using the structure of the feedback forcing. In the case of fluid flows, the quadratic nonlinearity is modeled as a structured forcing that is mapped by some unknown structured matrix, which is referred to as an uncertainty. Thus, the nonlinear dynamics of NSE can be modeled as an LTI system in feedback with a structured uncertainty [24–26]. We will show in the later sections that exploiting the structure of the quadratic nonlinearity for computing the gains not only leads to less conservative estimates of the I/O gain values but also leads to emergence of physically consistent modes identified in DNS studies that the resolvent framework does not capture, such as the lift-up mechanism, which was also identified for the smooth-wall case in [20]. Note that more refined estimates can be obtained by imposing additional structure of the quadratic nonlinearity and using specialized algorithms developed in [21, 22]; however, these refinements increase the computational expense and will not be considered in this preliminary investigation. Further comparison between the gains and modes computed using the relaxed and true structure of the nonlinearity are also given in [21, 22].

In this paper, we compute I/O gains and the related stability modes for a turbulent channel flow with rectangular and triangular riblets at the lower wall. We show that using the structure of the nonlinearity in modeling the feedback forcing yields less conservative I/O gain values as compared to the ones obtained using the traditional modeling of the forcing term i.e., resolvent analysis. Additionally, the structured I/O method allows for computing mode shapes that highlight various features of the velocity and forcing profiles, which provide better insight into the most sensitive directions for instability in the flow. We show that the I/O gains and modes obtained from the structured I/O method for the riblet cases highlight some of the instability mechanisms found in DNS studies such as the lift-up mechanism, Kelvin-Helmholtz (KH) vortices and Tollmien-Schlichting (TS) waves. Moreover, we compare the I/O gains for the riblet-based flow with the smooth-wall flow to ensure that the riblets minimize the I/O gains. The comparison highlights that the I/O gains associated with the NW modes are minimized by the riblets, however, the minimization leads to an increase in I/O gains for shorter structures that are consistent with the DNS predictions.

II. Turbulent Channel Flow Model

A. Perturbation Dynamics

Our goal is to assess the input-output stability of the incompressible turbulent channel flow model given a passive control device-such as a riblet-using the structured singular value (SSV) analysis. We start off with the following non-dimensionalized incompressible Navier-Stokes equation:

$$\mathbf{u}^t = \frac{1}{Re_\tau}\nabla^2\mathbf{u} - \nabla p - \mathbf{u} \cdot \nabla\mathbf{u}$$
$$\nabla \cdot \mathbf{u} = 0.$$

(1)

2

where $\mathbf{u} = [u, v, w]^T$ is the velocity vector, p is the pressure, Re_τ is the friction Reynolds number, $\nabla^2 = \partial_{xx} + \partial_{yy} + \partial_{zz}$ is the Laplacian and $\nabla = [\partial_x, \partial_y, \partial_z]^T$ is the gradient vector, respectively. Also, $\frac{\partial}{\partial j} = (\cdot)^j = \partial_j$ for any $j = x, y, z$ or t. We will use the $(\cdot)^j$ notation to represent the total derivative of quantities to improve the readability and interpretation of the equations. We model riblets by introducing a permeability function $K^{-1}(x, y, z)$ as an additional volume penalization term in (1) similar to the works [3, 4, 13]. This technique is synonymous to the fictitious domain method described in [27] to enforce the immersed boundary conditions for a solid obstacle. Thus, we have the following governing equation:

$$\mathbf{u}^t = \frac{1}{Re_\tau}\nabla^2\mathbf{u} - \nabla p - \mathbf{u} \cdot \nabla\mathbf{u} - K^{-1}\mathbf{u}$$

$$\nabla \cdot \mathbf{u} = 0. \tag{2}$$

Velocity and pressure terms can be decomposed into a base component and a perturbation about that base component. Hence, $\mathbf{u} = \mathbf{u}' + \mathbf{U}$ and $p = p' + P$, where $\mathbf{U}$ and P are the time-averaged mean velocity and pressure, and $\mathbf{u}'$ and p' are the perturbation velocity and pressure, respectively. Then, the perturbation and mean velocity equations are the following:

$$(\mathbf{u}')^t = \frac{1}{Re_\tau}\nabla^2\mathbf{u}' - \nabla p' - \mathbf{U} \cdot \nabla\mathbf{u}' - \mathbf{u}' \cdot \nabla\mathbf{U} - \mathbf{u}' \cdot \nabla\mathbf{u}' - K^{-1}\mathbf{u}' \tag{3a}$$

$$0 = -\nabla P - \mathbf{U} \cdot \nabla\mathbf{U} - K^{-1}\mathbf{U} + \frac{1}{Re_\tau}\nabla \cdot ((1 + \nu_T)(\nabla\mathbf{U} + (\nabla\mathbf{U})^T)) \tag{3b}$$

where $\mathbf{U} = [U_b, V_b, W_b]^T$ and ν_T is the eddy viscosity of the turbulent mean flow. The additional term containing the viscosity in (3b) represents the Reynolds stress. We will discuss modeling the mean flow and the Reynolds stress term in the later sections. For our analysis, we will assume K^{-1} and $\mathbf{U}$ to be streamwise constant with only wall-normal and spanwise variations, i.e., $\mathbf{U}(y, z)$ and $K^{-1}(y, z)$. Additionally, we will assume zero mean flow components in wall-normal and spanwise directions, thus, $\mathbf{U}(y, z) = \begin{bmatrix} U_b(y, z) & 0 & 0 \end{bmatrix}^T$. Note that variations in wall-normal and spanwise directions for the permeability function are associated with the width and spacing of the riblets, respectively. Thus, rectangular riblets have a constant width along the y direction, whereas, other geometries such as triangular riblets have a linearly varying width. Moving forward, we will omit $(')$, and U_b and K^{-1} dependence on y and z for conciseness. Additionally, we will model the convective nonlinearity as a forcing term denoted by $\mathbf{f}$ i.e., $\mathbf{f} = \mathbf{u} \cdot \nabla\mathbf{u} = \begin{bmatrix} f_x & f_y & f_z \end{bmatrix}^T$, where f_x, f_y and f_z are the forcings in streamwise, wall-normal and spanwise directions, respectively. Finally, we have the following perturbation equations:

$$\mathbf{u}^t = \frac{1}{Re_\tau}\nabla^2\mathbf{u} - \nabla p - U_b\mathbf{u}^x - (vU_b^y + wU_b^z)\mathbf{e}_x - \mathbf{f} - K^{-1}\mathbf{u}$$

$$\nabla \cdot \mathbf{u} = 0 \tag{4}$$

where $\mathbf{e}_x$ is the unit vector in the streamwise direction. We write equation 4 in the matrix form as

$$\mathbf{E}\psi^t = \mathbf{A}\psi + \mathbf{B}\mathbf{f} \tag{5}$$

where,

$$\mathbf{E} = \begin{bmatrix} I & 0 & 0 & 0 \\ 0 & I & 0 & 0 \\ 0 & 0 & I & 0 \\ 0 & 0 & 0 & 0 \end{bmatrix}$$

$$\psi = \begin{bmatrix} u \\ v \\ w \\ p \end{bmatrix}$$

$$\mathbf{A} = \begin{bmatrix} \frac{1}{Re_\tau}\nabla^2 - U_b\partial_x - K^{-1} & -U_b^y & -U_b^z & -\partial_x \\ 0 & \frac{1}{Re_\tau}\nabla^2 - U_b\partial_x - K^{-1} & 0 & -\partial_y \\ 0 & 0 & \frac{1}{Re_\tau}\nabla^2 - U_b\partial_x - K^{-1} & -\partial_z \\ \partial_x & \partial_y & \partial_z & 0 \end{bmatrix} \tag{6}$$

$$\mathbf{B} = \begin{bmatrix} -I & 0 & 0 \\ 0 & -I & 0 \\ 0 & 0 & -I \\ 0 & 0 & 0 \end{bmatrix}$$

$$\mathbf{f} = \begin{bmatrix} f_x \\ f_y \\ f_z \end{bmatrix}.$$

The last row in $\mathbf{A}$ enforces the incompressibility constraint, therefore, the last row in $\mathbf{E}$ is set to zero. This gives us the NSE in a descriptor form.

3

B. Turbulent Mean Flow

In this section, we will briefly discuss computing the turbulent mean profile. Recall that U_b and K^{-1} are streamwise constant functions with only wall-normal and spanwise variations. Thus, we will assume that U_b and K^{-1} are spanwise periodic functions with the same periodicity and can be represented by a Fourier series of the form

$$U_b(y,z) = \sum_{n=-\infty}^{\infty} U_n(y)e^{i(nk_s z)}$$

$$K^{-1}(y,z) = \sum_{n=-\infty}^{\infty} a_n(y)e^{i(nk_s z)}$$

(7)

where $U_n(y)$ and $a_n(y)$ are the Fourier coefficients with only wall-normal variations for the nth harmonic, s is the riblet spacing and $k_s = 2\pi/s$ is the spatial frequency. The coefficients $a_n(y)$ for riblets can be computed using the inverse fourier. We will use the equations in (3) and (7) to derive a bi-infinite matrix condition for mean flow calculations. Since $\mathbf{U} = [U_b(y,z), 0, 0]^{\text{T}}$, we can simplify the mean flow equation as the following:

$$0 = -ReP^x - ReK^{-1}U_b + v_T^y U_b^y + (1 + v_T)\nabla^2 U_b$$

(8)

Hence, the equation for n^{th} harmonic of U_b is given by:

$$[(v_T\partial_{yy} + v_T^y\partial_y)\delta(n) + \partial_{yy} - k_n^2 - (Re)a_0]U_n - Re\sum_{m\in\mathbb{Z}\backslash\{0\}} a_m U_{n-m} = ReP^x\delta(n)$$

(9)

where $\delta(n) = 1$ for $n = 0$ and $\delta(n) = 0$ for $n \neq 0$. Let $L_{n,0} = (v_T\partial_{yy} + v_T^y\partial_y)\delta(n) + \partial_{yy} - k_n^2 - (Re)a_0$. Then for $n = 0, \pm 1, \ldots, \pm 2n_h$, where n_h is some finite harmonic number of choice, we have the following:

$$
\begin{bmatrix}
L_{2n_h,0} & -(Re)a_1 & \cdots & \cdots & -(Re)a_{4n_h} \\
\vdots & \ddots & \vdots & \iddots & \vdots \\
\vdots & -(Re)a_{-1} & L_{0,0} & -(Re)a_1 & \vdots \\
\vdots & \iddots & \vdots & \ddots & \vdots \\
-(Re)a_{-4n_h} & \cdots & \cdots & -(Re)a_{-1} & L_{-2n_h,0}
\end{bmatrix}
\begin{bmatrix}
U_{2n_h} \\
\vdots \\
U_0 \\
\vdots \\
U_{-2n_h}
\end{bmatrix}
=
\begin{bmatrix}
\vdots \\
0 \\
ReP^x \\
0 \\
\vdots
\end{bmatrix}
$$

(10)

By simply solving (10), we can obtain various mean velocity modes. For analysis in this paper, the following eddy-viscosity v_T model for the turbulent channel flow is used:

$$v_T(y) = \frac{1}{2}\left(\sqrt{1 + \left(\frac{c_2}{3}Re(1 - y^2)(1 + 2y^2)(1 - e^{-\frac{(1-|y|)Re}{c_1}})\right)^2} - 1\right)$$

(11)

where c_1 and c_2 are parameters selected to minimize the deviations between experimental and simulation values of the mean streamwise velocity and the steady-state solution of (3b). The viscosity model given in (11) is described in detail by the authors in [28]. For the turbulent channel flow with $Re_\tau = 186$, $c_1 = 46.2$ and $c_2 = 0.61$ achieve the best fit to the mean velocity obtained in numerical simulations [29, 30]. For the turbulent channel flow with $Re_\tau = 547$, $c_1 = 29.4$ and $c_2 = 0.45$ obtains the best fit. Although equation (11) is not valid for riblets at the walls, we will use it to obtain an initial estimate of the mean velocity.

C. Spatial-Discretization and Numerical Implementation

1. Spatial-Discretization

In this section, we will briefly describe the spatial-discretization of the perturbation dynamics given in (5) and the construction of an input-output operator using those dynamics. First, we will discretize our system in $x - y - z$ directions using a Fourier-Chebyshev-Fourier basis. We will assume that the velocities have a periodic solution in temporal domain, and streamwise and spanwise directions. Thus, $\psi = \hat{\psi}(y)e^{i(\kappa_x x + \kappa_z z - \omega t)}$, where κ_x and κ_z are Fourier wavenumbers in streamwise and spanwise directions, ω is the temporal frequency and $\hat{\psi}(y)$ is the Fourier coefficient

4

discretized using the Chebyshev series for N collocation points in the wall-normal direction, respectively. Then, the equations in (31) can be written in the following form:

$$-i\omega\hat{\mathbf{E}}_{\mathbf{k},0}\hat{\psi}_{\mathbf{k}} = \hat{\mathbf{A}}_{\mathbf{k},0}\hat{\psi}_{\mathbf{k}} + \sum_{n\in\mathbb{Z}\backslash\{0\}}\hat{\mathbf{A}}_{\mathbf{k},n}\hat{\psi}_{\mathbf{k}+k_n} + \hat{\mathbf{B}}_{\mathbf{k}}\hat{\mathbf{f}}_{\mathbf{k}} \tag{12}$$

where

$$\hat{\mathbf{A}}_{\mathbf{k},0} = \begin{bmatrix} \frac{1}{Re_\tau}\hat{\nabla}^2 - U_0 i\kappa_x - a_0 & -\mathbf{D}U_0 & 0 & -i\kappa_x \\ 0 & \frac{1}{Re_\tau}\hat{\nabla}^2 - U_0 i\kappa_x - a_0 & 0 & -\mathbf{D} \\ 0 & 0 & \frac{1}{Re_\tau}\hat{\nabla}^2 - U_0 i\kappa_x - a_0 & -i\kappa_z \\ i\kappa_x & \mathbf{D} & i\kappa_z & 0 \end{bmatrix}$$

$$\hat{\mathbf{A}}_{\mathbf{k},n} = \begin{bmatrix} -U_n i\kappa_x - a_n & -\mathbf{D}U_n & -i\kappa_n U_n & 0 \\ 0 & -U_n i\kappa_x - a_n & 0 & 0 \\ 0 & 0 & -U_n i\kappa_x - a_n & 0 \\ 0 & 0 & 0 & 0 \end{bmatrix}$$

$$\hat{\mathbf{B}}_{\mathbf{k}} = \begin{bmatrix} -I & 0 & 0 \\ 0 & -I & 0 \\ 0 & 0 & -I \\ 0 & 0 & 0 \end{bmatrix}$$

$$\hat{\mathbf{E}}_{\mathbf{k}} = \begin{bmatrix} I & 0 & 0 & 0 \\ 0 & I & 0 & 0 \\ 0 & 0 & I & 0 \\ 0 & 0 & 0 & 0 \end{bmatrix}$$

$$\hat{\nabla}^2 = \mathbf{D}^2 - (\kappa_x^2 + \kappa_z^2).$$

Here, $\hat{\mathbf{A}}_{\mathbf{k},0} \in \mathbb{C}^{4N\times4N}$ and $\hat{\mathbf{A}}_{\mathbf{k},n} \in \mathbb{C}^{4N\times4N}$ are the linear system matrices, $\hat{\mathbf{B}}_{\mathbf{k}} \in \mathbb{C}^{4N\times3N}$ is the input matrix, $\hat{\mathbf{E}}_{\mathbf{k}} \in \mathbb{C}^{4N\times4N}$ is the mass matrix, $\hat{\psi}_{\mathbf{k}} \in \mathbb{C}^{4N}$ is the state vector, $\hat{\mathbf{f}}_{\mathbf{k}} \in \mathbb{C}^{3N}$ is the nonlinear forcing vector, $\mathbf{D} \in \mathbb{C}^{N\times N}$ is the discrete form of ∂_y computed using the methods in [31], $k_n = nk_s$ is the nth spatial frequency number, and $\mathbf{k} = \begin{bmatrix} \kappa_x & \kappa_z \end{bmatrix}$ and $\mathbf{k} + k_n = \begin{bmatrix} \kappa_x & \kappa_z + k_n \end{bmatrix}$ are wavenumber pairs for $n = 0$ and $n \neq 0$, respectively. Then, for $n = 0, \pm1, \ldots, \pm n_h$, we have the following equation:

$$
\begin{aligned}
&-i\omega\begin{bmatrix} \hat{\mathbf{E}}_{\mathbf{k}-n_h k_s} & 0 & \cdots & \cdots & 0 \\ 0 & \ddots & \ddots & \ddots & \vdots \\ \vdots & \vdots & \hat{\mathbf{E}}_{\mathbf{k}} & \ddots & \vdots \\ \vdots & \vdots & \ddots & \ddots & \vdots \\ 0 & \cdots & \cdots & 0 & \hat{\mathbf{E}}_{\mathbf{k}+n_h k_s} \end{bmatrix}\begin{bmatrix} \hat{\psi}_{\mathbf{k}-n_h k_s} \\ \vdots \\ \hat{\psi}_{\mathbf{k}} \\ \vdots \\ \hat{\psi}_{\mathbf{k}+n_h k_s} \end{bmatrix} = \begin{bmatrix} \hat{\mathbf{A}}_{\mathbf{k}-n_h k_s,0} & \hat{\mathbf{A}}_{\mathbf{k}-n_h k_s,1} & \cdots & \cdots & \hat{\mathbf{A}}_{\mathbf{k}-n_h k_s,2n_h} \\ \vdots & \ddots & \vdots & \ddots & \vdots \\ \vdots & \hat{\mathbf{A}}_{\mathbf{k},-1} & \hat{\mathbf{A}}_{\mathbf{k},0} & \hat{\mathbf{A}}_{\mathbf{k},1} & \vdots \\ \vdots & \ddots & \vdots & \ddots & \vdots \\ \hat{\mathbf{A}}_{\mathbf{k}+n_h k_s,-2n_h} & \cdots & \cdots & \hat{\mathbf{A}}_{\mathbf{k}+n_h k_s,-1} & \hat{\mathbf{A}}_{\mathbf{k}+n_h k_s,0} \end{bmatrix}\begin{bmatrix} \hat{\psi}_{\mathbf{k}-n_h k_s} \\ \vdots \\ \hat{\psi}_{\mathbf{k}} \\ \vdots \\ \hat{\psi}_{\mathbf{k}+n_h k_s} \end{bmatrix} \\
&+ \begin{bmatrix} \hat{\mathbf{B}}_{\mathbf{k}-n_h k_s} & 0 & \cdots & \cdots & 0 \\ 0 & \ddots & \ddots & \ddots & \vdots \\ \vdots & \vdots & \hat{\mathbf{B}}_{\mathbf{k}} & \ddots & \vdots \\ \vdots & \vdots & \ddots & \ddots & \vdots \\ 0 & \cdots & \cdots & 0 & \hat{\mathbf{B}}_{\mathbf{k}+n_h k_s} \end{bmatrix}\begin{bmatrix} \hat{\mathbf{f}}_{\mathbf{k}-n_h k_s} \\ \vdots \\ \hat{\mathbf{f}}_{\mathbf{k}} \\ \vdots \\ \hat{\mathbf{f}}_{\mathbf{k}+n_h k_s} \end{bmatrix}.
\end{aligned} \tag{13}
$$

Equation (13) can be concisely written as:

$$-i\omega\hat{\mathbf{E}}_{\mathbf{k}+}\hat{\psi}_{\mathbf{k}+} = \hat{\mathbf{A}}_{\mathbf{k}+}\hat{\psi}_{\mathbf{k}+} + \hat{\mathbf{B}}_{\mathbf{k}+}\hat{\mathbf{f}}_{\mathbf{k}+}. \tag{14}$$

where $\mathbf{k}+$ in the subscript denotes the coupled system of Fourier modes. To construct an input-output operator, we require an output equation such that $\hat{\mathbf{y}}_{\mathbf{k}+} = \hat{\mathbf{C}}_{\mathbf{k}+}\hat{\psi}_{\mathbf{k}+}$, where $\hat{\mathbf{C}}_{\mathbf{k}+} = \text{diag}(\hat{\mathbf{C}}_{\mathbf{k}-n_h k_s}, \ldots, \hat{\mathbf{C}}_{\mathbf{k}+n_h k_s})$ for any mapping $\hat{\mathbf{C}}_{\mathbf{k}+k_n} \in \mathbb{C}^{m\times2N}$ of compatible dimensions. Then, the input-output operator is the following:

$$\mathbf{M}_{\mathbf{k}+} = \hat{\mathbf{C}}_{\mathbf{k}+}(-i\omega\hat{\mathbf{E}}_{\mathbf{k}+} - \hat{\mathbf{A}}_{\mathbf{k}+})^{-1}\hat{\mathbf{B}}_{\mathbf{k}+}. \tag{15}$$

Note that $\mathbf{M}_{\mathbf{k}+} \in \mathbb{C}^{(2n_h+1)m\times(2n_h+1)3N}$ maps $\hat{\mathbf{f}}_{\mathbf{k}+} \in \mathbb{C}^{(2n_h+1)3N}$ onto $\hat{\mathbf{y}}_{\mathbf{k}+} \in \mathbb{C}^{(2n_h+1)m}$ i.e, $\hat{\mathbf{y}}_{\mathbf{k}+} = \mathbf{M}_{\mathbf{k}+}\hat{\mathbf{f}}_{\mathbf{k}+}$. We will use $\mathbf{M}_{\mathbf{k}+}$ to perform the structured input-output analysis to compute stability bounds and forcing/response mode shapes for (3) [21].

2. Numerical Implementation

The coefficients for the permeability function of K^{-1} in (7) are determined as

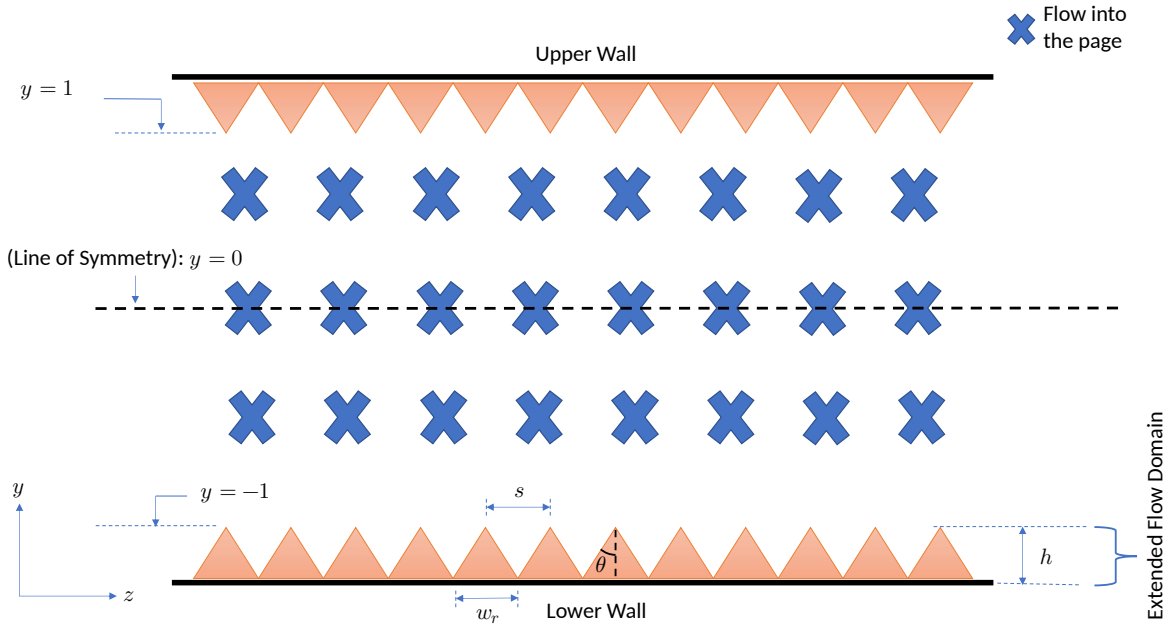$$a_n(y) = \frac{1}{\epsilon s^+}W(y)\sin\left(\frac{nk_s W(y)}{2}\right), \tag{16}$$

Fig. 1   Channel Flow setup

where ϵ is the Darcy resistance factor and

$$W(y) := w_r f(y)$$

is the width of the riblet as a function of y. Thus, $W(y)$ is constant for rectangular riblets and varies linearly for triangular riblets. Additionally, s^+ is the riblet spacing (s) given in viscous units i.e., $s^+ = sRe$. For numerical analysis, the rectangular riblet height and width is set to $h = 0.5s$ and $w_r = 0.25s$, and the triangular riblet height and width is set to $h = 0.5s/\tan(\theta)$ and $w_r = s$, respectively. Figure 1 illustrates a detailed setup of the channel flow system with riblets that we will utilize for our analysis.

   To reduce the computational load, we will use the symmetry of the channel flow configuration about $y = 0$ to construct $\mathbf{M_{k+}}$. Therefore, we will only consider the domain $y \in [-(1 + h), 0]$, where h is the riblet height with its tip at $y = -1$. Hence, we impose the symmetric boundary condition for all the velocity components. i.e.,

$$\frac{\partial \mathbf{u}}{\partial y}\bigg|_{y=0} = 0, \quad \frac{\partial U_n}{\partial y}\bigg|_{y=0} = 0. \tag{17}$$

Furthermore, we split the flow domain into two parts: unobstructed domain $y \in [-1, 0]$ and extended flow domain $y \in [-(1 + h), -1]$ (See Figure 1). This allows us to use different numbers of collocation points in each domain, which yields higher accuracy in results. However, the split domain introduces additional boundary conditions that must be enforced at the interface of the two domains:

$$\mathbf{u}|_{y=-1^+} = \mathbf{u}|_{y=-1^-}$$
$$p|_{y=-1^+} = p|_{y=-1^-}$$
$$U_n|_{y=-1^+} = U_n|_{y=-1^-} \tag{18}$$
$$\left(\frac{\partial u}{\partial y}\bigg|_{y=-1^+} - \frac{\partial u}{\partial y}\bigg|_{y=-1^-}\right)\mathbf{e}_x + \left(\frac{\partial w}{\partial y}\bigg|_{y=-1^+} - \frac{\partial w}{\partial y}\bigg|_{y=-1^-}\right)\mathbf{e}_z = 0.$$

The boundary conditions in (18) can be implemented using the rectangular operator discretization as described in [31]. We will use $N_o = 64$ collocation points in the unobstructed domain and $N_r = N_o/2$ points in the extended flow domain. Thus, $N = N_o + N_r$ are the total collocation points. Additionally, the harmonic values chosen for the analysis are $n = 0 \ldots \pm 6$, thus $n_h = 6$. The collocation points are chosen to ensure the convergence of singular values for the riblets-based flow to the ones obtained using the smooth-wall flow as $s^+ \to 0$. The N_o value chosen here is greater than

6

the one considered in [3] for resolvent analysis. The authors in [3] showed that their choice of $N_o = 54$ and $n_h = 6$ was sufficient to yield singular values that converged within $O(10^{-2})$ for the same model used here.

Furthermore, we impose Dirichlet boundary conditions at the lower-wall i.e., $\mathbf{u}|_{y=-(1+h)} = U_n|_{y=-(1+h)} = 0$. For all the results in this paper, we will use $Re_\tau = 180$ for the turbulent channel flow with $c_1 = 0.426$ and $c_2 = 25.4$ as coefficients for the viscosity profile. In this study, we will only consider small sized riblets and thus set $\nu_T = 0$ in the extended flow domain, since the flow is laminar near the walls of the channel. The complex nature of dynamical equations in (5) requires computing singular values for both the positive and negative frequency spectra, however, we confirmed from our analysis that only singular values corresponding to $\omega > 0$ yield physically meaningful structures. Thus, we only consider $\omega > 0$ for our analysis, which also consequently expedites the computations.

III. Structured Input-Output (I/O) Analysis

In this section, we will discuss the framework required for computing the I/O gain and associated forcing/response modes. We will describe these methods for a general complex matrix $\mathbf{H} \in \mathbb{C}^{r \times r}$, which corresponds to a frequency response matrix evaluated at a given frequency. Extension of the methods to the $\mathbf{M_{k+}}$ operator for the turbulent channel flow problem will be clear.

It is well-known that the convective nonlinearity in the incompressible NSE is quadratic in nature, which leads to the distribution of energy between velocity modes. This mixing of energy between various modes gives rise to the interactions between the nonlinear and linear dynamics of the incompressible NSE. This phenomena can be thought of as a nonlinear forcing term that is in feedback with the linear dynamics. The resolvent analysis uses this concept of a
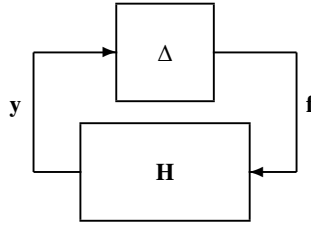

Fig. 2   Feedback interconnection of an uncertain system

feedback forcing to compute the I/O gain for an unstructured Δ, which is simply the maximum singular value of $\mathbf{H}$ i.e., $\|\mathbf{H}\|_2$, where $\| \cdot \|_2$ is the 2-norm of a matrix. Note that the energy-conserving property of the nonlinear forcing term is not imposed, however, the feedback nature of the forcing term is maintained. In the structured I/O analysis, additional to maintaining the feedback nature of this nonlinearity, we exploit its structure to compute the I/O gain. Thus, using the structure of the nonlinearity, we construct an uncertain LTI system as shown in 2 with the associated structured uncertainty Δ. The uncertainty-based LTI representation of NSE is described in [20], where the nonlinear term $\mathbf{u} \cdot \nabla \mathbf{u}$ is modelled as an input forcing $\mathbf{f} = [f_x, \ f_y, \ f_z]^T$ as the following:

$$\mathbf{f} = \mathbf{u} \cdot \nabla \mathbf{u} = \text{diag}(\mathbf{u}_\xi^T, \mathbf{u}_\xi^T, \mathbf{u}_\xi^T)\nabla \mathbf{u} = \Delta \nabla \mathbf{u} = \Delta \mathbf{y} \tag{19}$$

where $\text{diag}(\cdot)$ is a diagonal matrix, $\nabla = [\partial_x \ \partial_y \ \partial_z]^T$ is the gradient operator, and $\Delta \in \mathbf{\Delta}$ is the uncertainty associated with the linear system $\mathbf{H}$. Here, $\mathbf{\Delta} \subseteq \mathbb{C}^{r \times r}$ is the subset of structured complex matrices and $\mathbf{u}_\xi^T$ is an approximation of the velocity modeled as an unknown gain matrix. This Δ maps the outputs $\mathbf{y} = \nabla \mathbf{u}$ onto the forcing signals, which preserves the underlying structure of the nonlinearity. Note that the uncertainty Δ in (19) has a repeated complex full-block structure, which is a special class of structured uncertainties that require the use of algorithms described in [21, 22] to compute the I/O gains and mode shapes. However, computing the I/O gains and mode shapes for the repeated complex full-block structure is computationally intensive especially when the $\mathbf{M_{k+}}$ operator is a coupled system of Fourier modes. Thus, we will introduce a relaxation on Δ such that

$$\Delta \approx \text{diag}(\mathbf{u}_{\xi_1}^T, \mathbf{u}_{\xi_2}^T, \mathbf{u}_{\xi_3}^T) \tag{20}$$

where each $\mathbf{u}_{\xi_i} \in \mathbb{C}^{r_i \times r_i}$ for $i = 1, 2, 3$ is an approximation of $\mathbf{u}_\xi$ given in (19). This approximation allows us to retain the block-diagonal concatenation of the underlying structured Δ and also use fast-converging iterative schemes to obtain I/O gains. Although the relaxation introduces some degree of conservatism in the I/O gain values in exchange for

7

computational speed, the relaxed Δ is still more physically consistent with the structure of the nonlinearity than the unstructured Δ assumed in the traditional resolvent analysis. We will show later in the results section that incorporating the relaxed Δ in the analysis yields less conservative bounds than the traditional resolvent analysis.

A. Input-Output Gain

The input-output gain of an LTI system with a structured uncertainty is computed as the following:

$$\mu_{\Delta}(\mathbf{H}) := \frac{1}{\min(\|\Delta\|_2 : \Delta \in \mathbf{\Delta}, \det(\mathbf{I}_r - \mathbf{H}\Delta) = 0)}. \tag{21}$$

where $\mu_{\Delta}(\mathbf{H})$ is called the structured singular value of $\mathbf{H}$. Thus, for any $\mathbf{H}$ with an uncertainty Δ, equation (21) can be solved to obtain the SSV. In practice, a convex upper bound problem is solved in lieu of directly solving (21) because the exact solution for a given Δ is NP-Hard [32, 33]. However, for some uncertainty structures, as noted in the works of [25, 34, 35], the convex upper bound and $\mu_{\Delta}(\mathbf{H})$ are equal. Thus, the upper bound problem is written in the following form:

$$\mu_{\Delta}(\mathbf{H}) \leq \min \|\mathbf{DHD}^{-1}\|_2. \tag{22}$$

where $\mathbf{D} \in \mathbb{D}$ is a scaling matrix such that $\mathbf{D}\Delta = \Delta\mathbf{D}$ and $\mathbb{D}$ is a set of non-singular "commuting" matrices [25, 36]. It is important to note that $\det(\mathbf{I}_r - \mathbf{H}\Delta) = \det(\mathbf{I}_r - \mathbf{DHD}^{-1}\Delta)$ and consequently, $\mu_{\Delta}(\mathbf{H}) = \mu_{\Delta}(\mathbf{DHD}^{-1})$. This is known as the D-scale upper bound and there are various algorithms that can solve this problem [37–39]. However, solving the minimization problem on the right-hand side of (22) tends to scale poorly with large dimensioned problems, as is the case here. Thus, we will utilize a weaker bound, i.e., $\min \|\mathbf{DHD}^{-1}\|_2 \leq \min \|\mathbf{DHD}^{-1}\|_F$, where $\|\cdot\|_F$ is the Frobenius norm of a matrix. The Frobenius norm minimization can be solved using a fast-converging iterative algorithm known as the Osborne's iteration [40]. Particularly, we will use the version of Osborne's iteration that solves for $\mathbf{D} \in \mathbb{D}$ such that $\mathbb{D} := \{\text{diag}(d_1\mathbf{I}_1, d_2\mathbf{I}_2, d_3\mathbf{I}_3) : d_i \in \mathbb{R}, d_i > 0\}$, where $r = \sum_{i=1}^3 r_i$. Further details about the algorithm that computes $\mathbf{D}$ are given in [21, 22]. The weaker bound implicitly enforces the approximation given in (20). The upper bound is computed as $\|\hat{\mathbf{H}}\|_{\mu} = \|\mathbf{DHD}^{-1}\|_2$, where $\mathbf{D}$ minimizes $\|\mathbf{DHD}\|_F$. We will refer to $\|\hat{\mathbf{H}}\|_{\mu}$ as the I/O gain of $\mathbf{H}$. Note that larger values of $\|\hat{\mathbf{H}}\|_{\mu}$ indicate higher sensitivity of the system to perturbations in the presence of a structured Δ, which is a consequence of the small-gain theorem [41]. The stability margin can be computed by taking the inverse of $\|\hat{\mathbf{H}}\|_{\mu}$.

B. Input-Output modes

Following from our discussion of the I/O gain computation, the associated I/O modes are computed using a standard power-iteration algorithm [21, 25]. In general, the power-iteration algorithm seeks the smallest uncertainty Δ by solving the following problem:

$$\begin{aligned} \max \ & \rho(\Delta\mathbf{H}) \\ \text{subject to}: \ & \det(\mathbf{I}_r - \mathbf{H}\Delta) = 0 \end{aligned} \tag{23}$$

where $\rho(\cdot)$ is the spectral radius. The determinant condition in (23) is equivalent to finding $\Delta \in \mathbf{\Delta}$ such that $\mathbf{y} = \mathbf{Hf}$ and $\mathbf{f} = \Delta\mathbf{y}$, where $\mathbf{f} \in \mathbb{C}^r$ and $\mathbf{y} \in \mathbb{C}^r$ are input forcing and outputs, respectively. This can be done by using the power-iteration. Generally, the power-iteration does not find the smallest uncertainty, however, it yields a lower bound $\beta = \frac{1}{\|\Delta\|_2}$ such that $\mu_{\Delta}(\mathbf{H}) \geq \beta$, which provides a sufficient condition for instability. Thus, the lower-bound can be computed by iterating through the following equations using any unit signals $\mathbf{b} \in \mathbb{C}^r$ and $\mathbf{w} \in \mathbb{C}^r$:

$$\beta\mathbf{a} = \mathbf{Hb} \tag{24a}$$

$$\mathbf{z}_1 = \frac{\|\mathbf{w}_1\|_2}{\|\mathbf{a}_1\|_2}\mathbf{a}_1, \ \mathbf{z}_2 = \frac{\|\mathbf{w}_2\|_2}{\|\mathbf{a}_2\|_2}\mathbf{a}_2, \ \mathbf{z}_3 = \frac{\|\mathbf{w}_3\|_2}{\|\mathbf{a}_3\|_2}\mathbf{a}_3 \tag{24b}$$

$$\beta\mathbf{w} = \mathbf{H}^{\mathrm{H}}\mathbf{z} \tag{24c}$$

$$\mathbf{b}_1 = \frac{\|\mathbf{a}_1\|_2}{\|\mathbf{w}_1\|_2}\mathbf{w}_1, \ \mathbf{b}_2 = \frac{\|\mathbf{a}_2\|_2}{\|\mathbf{w}_2\|_2}\mathbf{w}_2, \ \mathbf{b}_3 = \frac{\|\mathbf{a}_3\|_2}{\|\mathbf{w}_3\|_2}\mathbf{w}_3 \tag{24d}$$

where $\mathbf{a}_i, \mathbf{z}_i, \mathbf{b}_i, \mathbf{w}_i \in \mathbb{C}^{r_i}$ are compatibly partitioned signals for $i = 1, 2, 3$. Note that (24d) gives $\|\mathbf{b}_i\|_2 = \|\mathbf{a}_i\|_2$ for $i = 1, 2, 3$. Thus, there exists $\mathbf{Q}_i \in \mathbb{C}^{r_i \times r_i}$ such that $\|\mathbf{Q}_i\|_2 = 1$ and $\mathbf{b}_i = \mathbf{Q}_i\mathbf{a}_i$. Then, define $\mathbf{f} = \mathbf{b}$, $\mathbf{y} = \beta\mathbf{a}$ and $\Delta = \frac{1}{\beta}\text{diag}(\mathbf{Q}_1, \mathbf{Q}_2, \mathbf{Q}_3)$ as the forcing modes, response modes and structured uncertainty of the system, respectively. It

8

can be verified from (24a) that $\mathbf{y} = \mathbf{Hf}$. Thus, the associated signals $\mathbf{f}$ and $\mathbf{y}$ are the destabilizing modes of $\mathbf{H}$. Further details about the power-iteration algorithms that compute the lower bounds and the associated signals are given in [22, 25]. When upper and lower bounds are sufficiently tight (e.g., within 5% of each other) then simply computing the right and left singular vectors of $\mathbf{DHD}^{-1}$ using a singular value decomposition (SVD) will produce nearly identical modes $\mathbf{f}$ and $\mathbf{y}$ to the ones from the power-iteration [21]. The modes are determined as $\mathbf{y} = \mathbf{D}^{-1}\mathbf{u}_1$ and $\mathbf{f} = \mathbf{D}^{-1}\mathbf{v}_1$, where $\mathbf{u}_1$ and $\mathbf{v}_1$ are the left and right singular vectors associated with the largest singular value of $\mathbf{DHD}^{-1}$.

IV. Results

In this section, we briefly comment on the interpretation of the I/O gains and modes generated from the structured I/O analysis using the relaxed Δ defined in 20. Additionally, we will showcase the I/O gains and mode shapes for two types of riblets: rectangular and triangular riblets. We will show that using a structured Δ (despite the relaxation) yields less conservative estimates of the I/O gains and highlights important structures/mode shapes that are consistent with the ones found in the fluids literature.

A. Computational Parameters

We will show results for smooth wall, triangular and rectangular riblets with spacing in viscous units set to $s^+ = 23$, which is considered to be the optimal spacing for minimizing the effect of the near-wall (NW) cycle [3]. The triangular riblets have a tip half-angle of $30°$. We will use a $50 \times 50 \times 21$ grid of $n_{\lambda_x^+} \times n_{\lambda_z^+} \times n_{c^+}$ to compute the I/O gains, where $n_{\lambda_x^+}$, $n_{\lambda_z^+}$ and n_{c^+} are total grid points for streamwise length (λ_x^+), spanwise length (λ_z^+) and wave speed (c^+), respectively. Here, $\lambda_x^+ = \frac{2\pi Re}{\kappa_x}$, $\lambda_z^+ = \frac{2\pi Re}{\kappa_z}$ and $c^+ = \omega/\kappa_x$, where κ_x and κ_z are streamwise and spanwise wavenumbers, respectively. We use logrithmically spaced values $\lambda_x^+ = [10^{0.5}, \ 10^{4.5}]$ and $\lambda_z^+ = [10^{0.5}, \ 10^{4.5}]$, and linearly-spaced $c^+ = [4, \ 40]$ for all the results in this section. The length-scales values were chosen to contain the wavenumbers that are in the high-energy spectra as indicated in [42]. We will compute $\|\hat{\mathbf{M}}_{\mathbf{k}+}\|_2$, $\|\hat{\mathbf{M}}_{\nabla_{\mathbf{k}+}}\|_2$ and $\|\hat{\mathbf{M}}_{\nabla_{\mathbf{k}+}}\|_\mu$ over a spectrum of length-scale pairs $(\lambda_x^+, \lambda_z^+)$ and wave-speeds c^+, where $\hat{\mathbf{M}}_{\mathbf{k}+}$ and $\hat{\mathbf{M}}_{\nabla_{\mathbf{k}+}}$ have $\hat{\mathbf{y}}_{\mathbf{k}+} = \hat{\mathbf{u}}_{\mathbf{k}+}$ and $\hat{\mathbf{y}}_{\nabla_{\mathbf{k}+}} = \hat{\nabla}\hat{\mathbf{u}}_{\mathbf{k}+}$ as the outputs, respectively. Recall that choosing $\hat{\mathbf{y}}_{\nabla_{\mathbf{k}+}} = \hat{\nabla}\hat{\mathbf{u}}_{\mathbf{k}+}$ as the outputs establishes the feedback interconnection between the system $\hat{\mathbf{M}}_{\nabla_{\mathbf{k}+}}$ and Δ i.e, $\hat{\mathbf{y}}_{\nabla_{\mathbf{k}+}} = \hat{\mathbf{M}}_{\nabla_{\mathbf{k}+}}\hat{\mathbf{f}}_{\mathbf{k}+}$ and $\hat{\mathbf{f}}_{\mathbf{k}+} = \Delta\hat{\mathbf{y}}_{\nabla_{\mathbf{k}+}}$. The "best" gain is the maximum value computed over the range of wave-speeds at a fixed wavenumber pair, which is identical to computing the H_∞ norm of a system. Note that $\|\hat{\mathbf{M}}_{\mathbf{k}+}\|_2$ is simply the resolvent of a matrix since no structure is imposed on Δ [3, 6].

B. Discussion

1. Smooth Wall

We will first discuss the smooth wall case to provide some physical insights for the I/O gain values and mode-shapes without any effect of the riblets. The plots shown in figure 3(a) and 3(b) are the resolvent gains obtained using the traditional resolvent methods described in [3], which is simply taking the maximum singular value of the I/O operators $\hat{\mathbf{M}}_{\mathbf{k}+}$ and $\hat{\mathbf{M}}_{\nabla_{\mathbf{k}+}}$. Thus, we do not assume any structure on Δ when computing the I/O gains in figures 3(a) and 3(b). Additionally, note that $\hat{\mathbf{M}}_{\mathbf{k}+}$ and $\hat{\mathbf{M}}_{\nabla_{\mathbf{k}+}}$ highlight the same regions when $\| \cdot \|_2$ values are computed, however, $\hat{\mathbf{M}}_{\nabla_{\mathbf{k}+}}$ has higher gain values comparatively. The difference in gains is mainly because we use gradients of velocities as outputs for $\hat{\mathbf{M}}_{\nabla_{\mathbf{k}+}}$ instead of just the velocities. This difference is consistent throughout all the smooth-wall and riblet-wall computations. However, when the structure of the Δ is imposed, the I/O gains decrease by an order of magnitude than the ones predicted using the resolvent analysis of the $\hat{\mathbf{M}}_{\nabla_{\mathbf{k}+}}$ operator. We can clearly see in figure 3(c) that the I/O gains are much smaller than the ones in figures 3(a) and 3(b). Additionally, the distribution of the I/O gains is also different, which highlights different regions of the gain values that are most sensitive to perturbations.

The black circles on the figures indicate the length-scales associated with the structures highlighted by the two analyses. We can see that the structures highlighted by the resolvent framework indicate long streamwise-oriented structures with $\lambda_x^+ = 3.16 \times 10^4$, $\lambda_z^+ = 4.19 \times 10^2$ and $c^+ = 16.6$ that are most common with spanwise perturbations. On the contrary, the SSV method in figure 3(c) highlights $\lambda_x^+ = 4 \times 10^3$, $\lambda_z^+ = 8.9 \times 10^2$ and $c^+ = 16.6$ as the most dominant structure that will cause instability. The length-scales highlighted using the SSV method are indicative of a lift-up mechanism with structures that are oblique, which have been documented as being most sensitive to transitioning to turbulence in the laminar direct numerical simulation (DNS) studies [20]. We can compute the structures directly using the power-iteration defined for the I/O modes. We can see in figure 7(a) that the analysis predicts the lift-up mechanism and the structures shown in figure 7(b) are oblique. Furthermore, we can compare the velocity and forcing modes at

9

$\lambda_x^+ = 4 \times 10^3$, $\lambda_z^+ = 8.9 \times 10^2$ and $c^+ = 16.6$ between the power-iteration and the resolvent SVD as shown in figures 5(a) and 5(b). We can see that the dominant forcing modes are different between the two methods with streamwise forcing being the most dominant when using the power-iteration as compared to the spanwise forcing in the resolvent SVD case. However, the velocity modes are nearly identical between the two methods.

(a) $\log_{10}(\|\hat{\mathbf{M}}_{\kappa+}\|_2)$ (b) $\log_{10}(\|\hat{\mathbf{M}}_{\nabla_{\kappa+}}\|_2)$ (c) $\log_{10}(\|\hat{\mathbf{M}}_{\nabla_{\kappa+}}\|_\mu)$

(d) $\log_{10}(\|\hat{\mathbf{M}}_{\kappa+}\|_2)$ (e) $\log_{10}(\|\hat{\mathbf{M}}_{\nabla_{\kappa+}}\|_2)$ (f) $\log_{10}(\|\hat{\mathbf{M}}_{\nabla_{\kappa+}}\|_\mu)$

(g) $\log_{10}(\|\hat{\mathbf{M}}_{\kappa+}\|_2)$ (h) $\log_{10}(\|\hat{\mathbf{M}}_{\nabla_{\kappa+}}\|_2)$ (i) $\log_{10}(\|\hat{\mathbf{M}}_{\nabla_{\kappa+}}\|_\mu)$
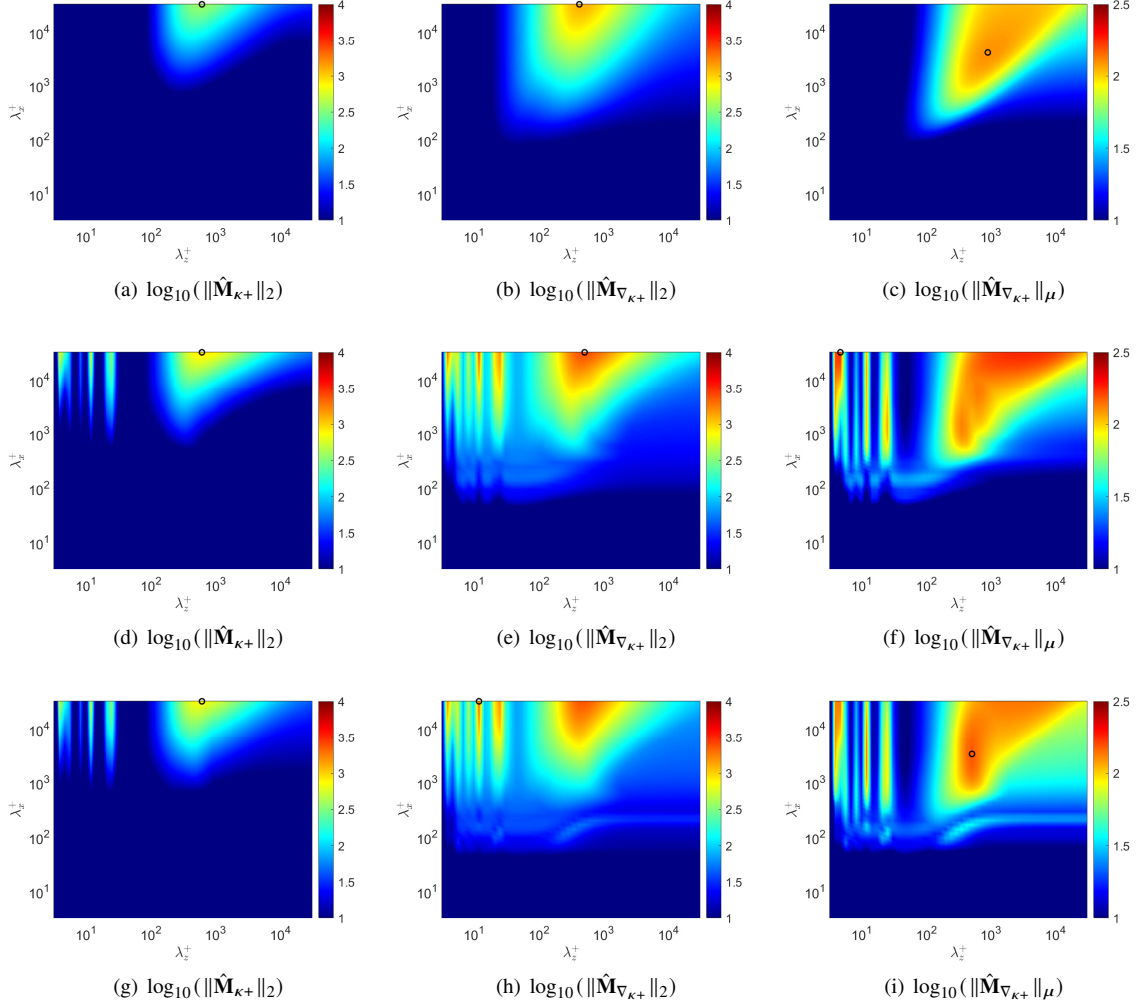
Fig. 3   (Top Row) Smooth-wall, (Middle Row) Triangular-Riblets, (Bottom Row) Rectangular-Riblets. The black circles indicate the regions with the largest value of the heat map.

2. Triangular Riblets: $s^+ = 23$

Now, consider the case with triangular riblets that are equally spaced with $s^+ = 23$. Similar to the smooth wall cases, the resolvent framework highlights streamwise dominant structures as compared to the SSV method. We can clearly see in figure 3(d) and 3(e) that the hot-spots are most concentrated in the regions with $\lambda_x^+ \geq 10^4$ and $10^{2.5} \leq \lambda_z^+ \leq 10^3$. On the contrary, the SSV analysis highlights structures around $\lambda_x^+ \leq 10^4$ and $10^{2.5} \leq \lambda_z^+ \leq 10^3$ in addition to the ones highlighted by the resolvent framework. Moreover, the I/O gains are much smaller for the SSV framework as compared to the resolvent framework. However, the presence of riblets induces additional instabilities for $\lambda_x^+ \geq 1 \times 10^2$ and $\lambda_z^+ \leq 35$ with maximum value $\|\hat{\mathbf{M}}_{\nabla_{\kappa+}}\|_\mu = 1.8 \times 10^2$ at $\lambda_x^+ = 3.16 \times 10^4$, $\lambda_z^+ = 4.61$ and $c^+ = 20.2$ as indicated by the black circle in figure 3(f). This value is an order of magnitude smaller than the largest value $\|\hat{\mathbf{M}}_{\nabla_{\kappa+}}\|_2 = 2.48 \times 10^3$ obtained from the resolvent framework at $\lambda_x^+ = 3.16 \times 10^4$, $\lambda_z^+ = 5.05 \times 10^2$ and $c^+ = 20.2$ in figure 3(e). Both methods

highlight streamwise oriented structures with $\|\hat{\mathbf{M}}_{\nabla_{\kappa+}}\|_\mu$ plot highlighting thin and long structures as compared to the thick and long structures highlighted from the $\|\hat{\mathbf{M}}_{\nabla_{\kappa+}}\|_2$ plot. Moreover, at the same grid point of $\lambda_x^+ = 3.16 \times 10^4$, $\lambda_z^+ = 4.61$ and $c^+ = 20.2$, where we obtain the maximum I/O gain $\|\hat{\mathbf{M}}_{\nabla_{\kappa+}}\|_\mu$, the resolvent gain is $\|\hat{\mathbf{M}}_{\nabla_{\kappa+}}\|_2 = 5.12 \times 10^2$, which is almost 2.75 times the largest $\|\hat{\mathbf{M}}_{\nabla_{\kappa+}}\|_\mu$ value. If we compare the mode shapes at this grid point as shown in figures 5(c) and 5(d), we will see that $\|\hat{\mathbf{M}}_{\nabla_{\kappa+}}\|_2$ indicates spanwise dominant forcing modes as opposed to streamwise dominant forcing modes for $\|\hat{\mathbf{M}}_{\nabla_{\kappa+}}\|_\mu$. Interestingly, the structures highlighted around $\lambda_x^+ \le 10^4$ and $10^{2.5} \le \lambda_z^+ \le 10^3$ have comparable $\|\hat{\mathbf{M}}_{\nabla_{\kappa+}}\|_\mu$ magnitudes to the maximum value indicated in figure 3(f). Thus, the SSV analysis highlights secondary structures/mechanisms that are important and sensitive to perturbations.

Compared to the smooth wall case in figure 3(c), the heat map in figure 3(f) indicates that having riblets further destabilizes the system since the $\|\hat{\mathbf{M}}_{\nabla_{\kappa+}}\|_\mu$ values are larger for the riblets case. Recall that the heat-map in figure 3(f) is the maximum over the grid of c^+ values. Thus, the plot does not show $\|\hat{\mathbf{M}}_{\nabla_{\kappa+}}\|_\mu$ values for the rest of the c^+ grid. For example, if we compare the $\|\hat{\mathbf{M}}_{\nabla_{\kappa+}}\|_\mu$ values as shown in figures 4(a), 4(b) and 4(c) at the grid point indicated in [3] to be commonly associated with the NW cycle i.e., $\lambda_x^+ \approx 10^3$, $\lambda_z^+ \approx 10^2$ and $c^+ = 9.4$, then the triangular riblets decrease the I/O gain by approximately 40%. The peak is suppressed by the riblets and instead we get a shift in the structures with a weaker peak at $\lambda_x^+ \approx 10^2$ and $\lambda_z^+ \approx 10^2$. However, this does not forego the fact that the riblets can potentially cause instabilities at other c^+ values, which is precisely indicated by the figure in 3(f) and is not found through the resolvent analysis in figure 3(e). Lastly, the c^+ grid values that lead to large $\|\hat{\mathbf{M}}_{\nabla_{\kappa+}}\|_\mu$ values are approximately in the range $18.4 \le c^+ \le 20.2$ as shown in figure 6(b). The wave speeds $18.4 \le c^+ \le 18.64$ obtained from the SSV analysis are within ± 2.14 of the baseflow centerline values used for the DNS study in [42] to compare the dissipation energy spectra of different DNS databases.

3. Rectangular Riblets: $s^+ = 23$

To further depict the generality of the method, we will consider rectangular riblets with $s^+ = 23$. The $\|\hat{\mathbf{M}}_{\nabla_{\kappa+}}\|_\mu$ values between the triangular and rectangular riblets are qualitatively similar. However, these values differ quantitatively with 34.44% of $\|\hat{\mathbf{M}}_{\nabla_{\kappa+}}\|_\mu$ values for the rectangular riblets being on average 8.29% less than the triangular riblets case indicated in the figures 3(f) and 3(i), respectively. The triangular riblets are better at minimizing the I/O gains than the rectangular riblets for 65.56% of the grid points with an average reduction in I/O gains of 24.45%.

Similar to the smooth wall case, the largest value $\|\hat{\mathbf{M}}_{\nabla_{\kappa+}}\|_\mu = 151.4407$ occurs at $\lambda_x^+ = 3.31 \times 10^3$, $\lambda_z^+ = 5.05 \times 10^2$ and $c^+ = 18.4$, which indicates oblique structures and a lift-up mechanism as shown in figures 7(c) and 7(d). On the contrary, the resolvent analysis yields $\|\hat{\mathbf{M}}_{\nabla_{\kappa+}}\|_2 = 2.41 \times 10^3$ occurring at $\lambda_x^+ = 3.16 \times 10^4$, $\lambda_z^+ = 1.17 \times 10^1$ and $c^+ = 18.4$, which is an indication of a streamwise dominant structures. For $\lambda_x^+ = 3.31 \times 10^3$, $\lambda_z^+ = 5.05 \times 10^2$ and $c^+ = 18.4$, the I/O gain $\|\hat{\mathbf{M}}_{\nabla_{\kappa+}}\|_2 = 3.76 \times 10^2$, which more than twice the largest $\|\hat{\mathbf{M}}_{\nabla_{\kappa+}}\|_\mu$ value. Similar to the other cases, the forcing modes computed at the largest value of $\|\hat{\mathbf{M}}_{\nabla_{\kappa+}}\|_\mu$ are different between the power-iteration and the resolvent SVD as shown in figures 5(c) and 5(d). Power-iteration results in streamwise dominant forcing modes as compared to the spanwise dominant forcing modes from the resolvent SVD.

Furthermore, we observe in figure 3(i) that the rectangular riblets induce TS instabilities, which are evident from the band of $\|\hat{\mathbf{M}}_{\nabla_{\kappa+}}\|_\mu$ values for $\lambda_x^+ \approx 10^2$ and $\lambda_z^+ > 10^2$. Similar trend is seen in figure 3(h), however, the TS-band is not as dominating. Observe that the $\|\hat{\mathbf{M}}_{\nabla_{\kappa+}}\|_\mu$ values in figure 6(c) indicate KH vortices for $\lambda_x^+ = 1.36 \times 10^2$ and $c^+ = 4$. We can see in figure 8(a) that we indeed have KH vortices forming just above the tips of the rectangular riblets for $\lambda_x^+ = 1.36 \times 10^2$, $\lambda_z^+ = 3.47 \times 10^2$ and $c^+ = 4$. The mode shapes in figures 8(b) and 8(c) also indicate that the largest momentum occurs at $y \approx -1$. Furthermore, the length-scales $\lambda_x^+ = 1.36 \times 10^2$ and $\lambda_z^+ = 3.47 \times 10^2$ associated with KH vortices exactly lie at the hotspot of TS-band shown in figure 3(i). These vortical structures tend to be weaker for the triangular riblets, which is correctly predicted by the $\|\hat{\mathbf{M}}_{\nabla_{\kappa+}}\|_\mu$ values for $\lambda_x^+ = 1.36 \times 10^2$ and $c^+ < 5$ in 6(b), which is consistent with the DNS results [43].

(a) $\log_{10}(\|\hat{\mathbf{M}}_{\nabla_{\kappa+}}\|_{\mu})$ (Smooth-Wall)

(b) $\log_{10}(\|\hat{\mathbf{M}}_{\kappa+}\|_{\mu})$ (Triangular Riblets)

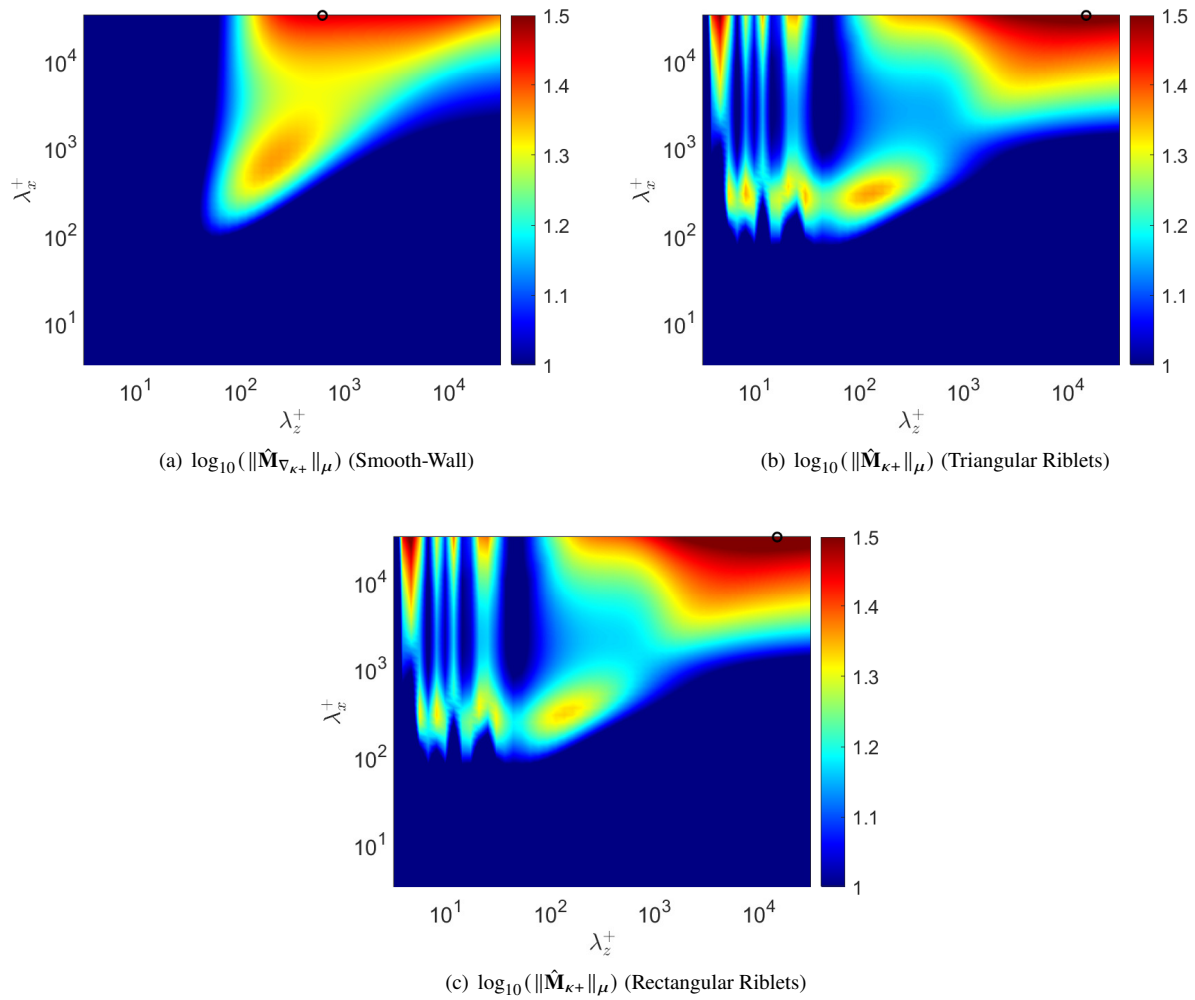(c) $\log_{10}(\|\hat{\mathbf{M}}_{\kappa+}\|_{\mu})$ (Rectangular Riblets)

Fig. 4 **The plots depict the I/O gains at $c^+ = 9.4$ over all the length-scales. We see that around the length-scales most common for near-wall cycle $\lambda_x^+ \approx 10^3$ and $\lambda_z^+ \approx 10^2$, the I/O gains reduce by approximately 40% for both riblets.**
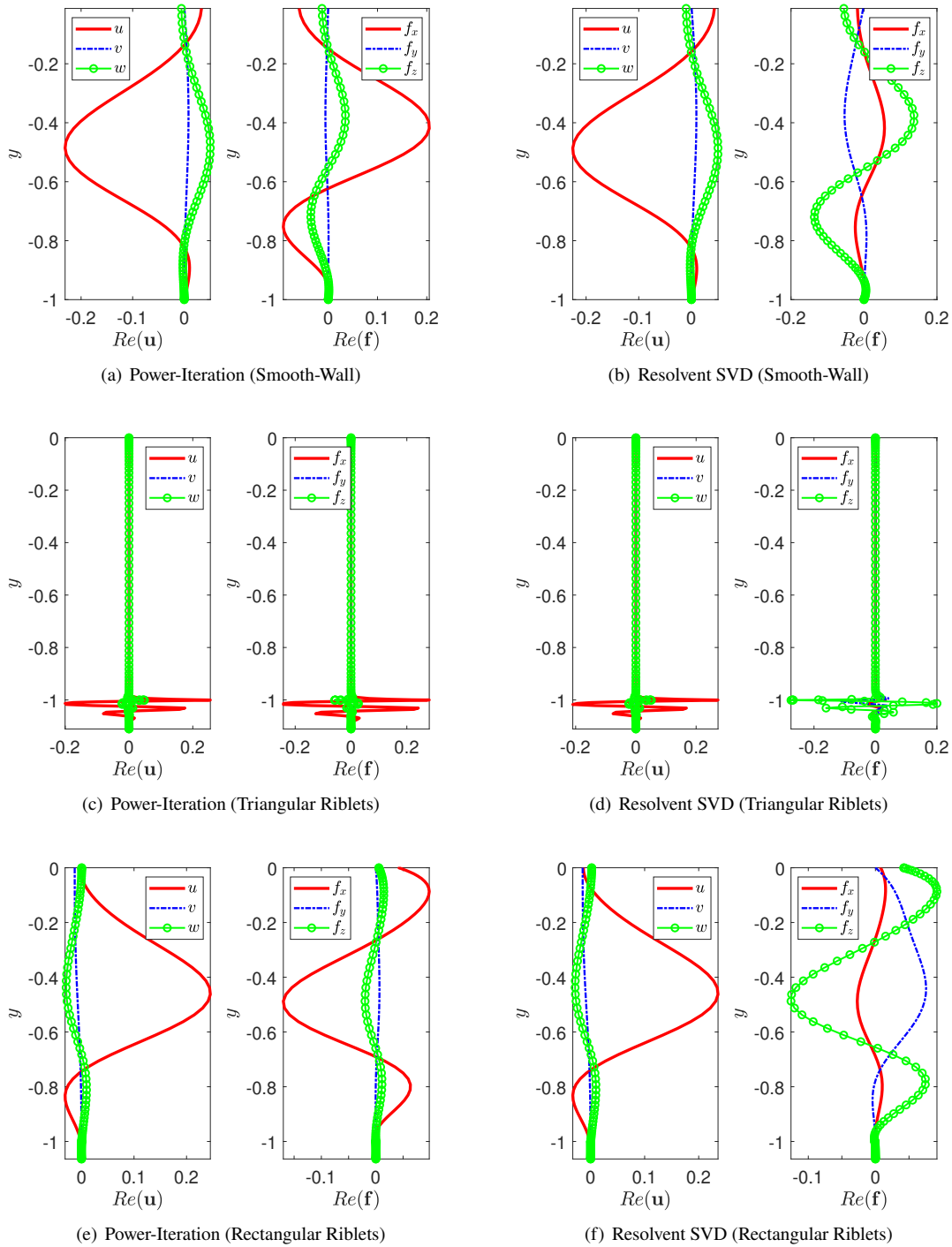
(a) Power-Iteration (Smooth-Wall)

(b) Resolvent SVD (Smooth-Wall)

(c) Power-Iteration (Triangular Riblets)

(d) Resolvent SVD (Triangular Riblets)

(e) Power-Iteration (Rectangular Riblets)

(f) Resolvent SVD (Rectangular Riblets)

Fig. 5 The plots depict mode shapes obtained using the power-iteration (Left) and the resolvent SVD (Right) for c^+, λ_x^+ and λ_z^+ values corresponding to the largest $\|\hat{\mathbf{M}}_{\nabla_{\kappa+}}\|_\mu$ for each setup. We only plot the real parts of the velocity and forcing modes. Additionally, the signals $\mathbf{f}$ and $\mathbf{u}$ are unit norm.

13

(a) $\log_{10}(\|\hat{\mathbf{M}}_{\nabla_{\kappa+}}\|_{\mu})$ (Smooth-Wall)

(b) $\log_{10}(\|\hat{\mathbf{M}}_{\nabla_{\kappa+}}\|_{\mu})$ (Triangular Riblets)

(c) $\log_{10}(\|\hat{\mathbf{M}}_{\nabla_{\kappa+}}\|_{\mu})$ (Rectangular Riblets)
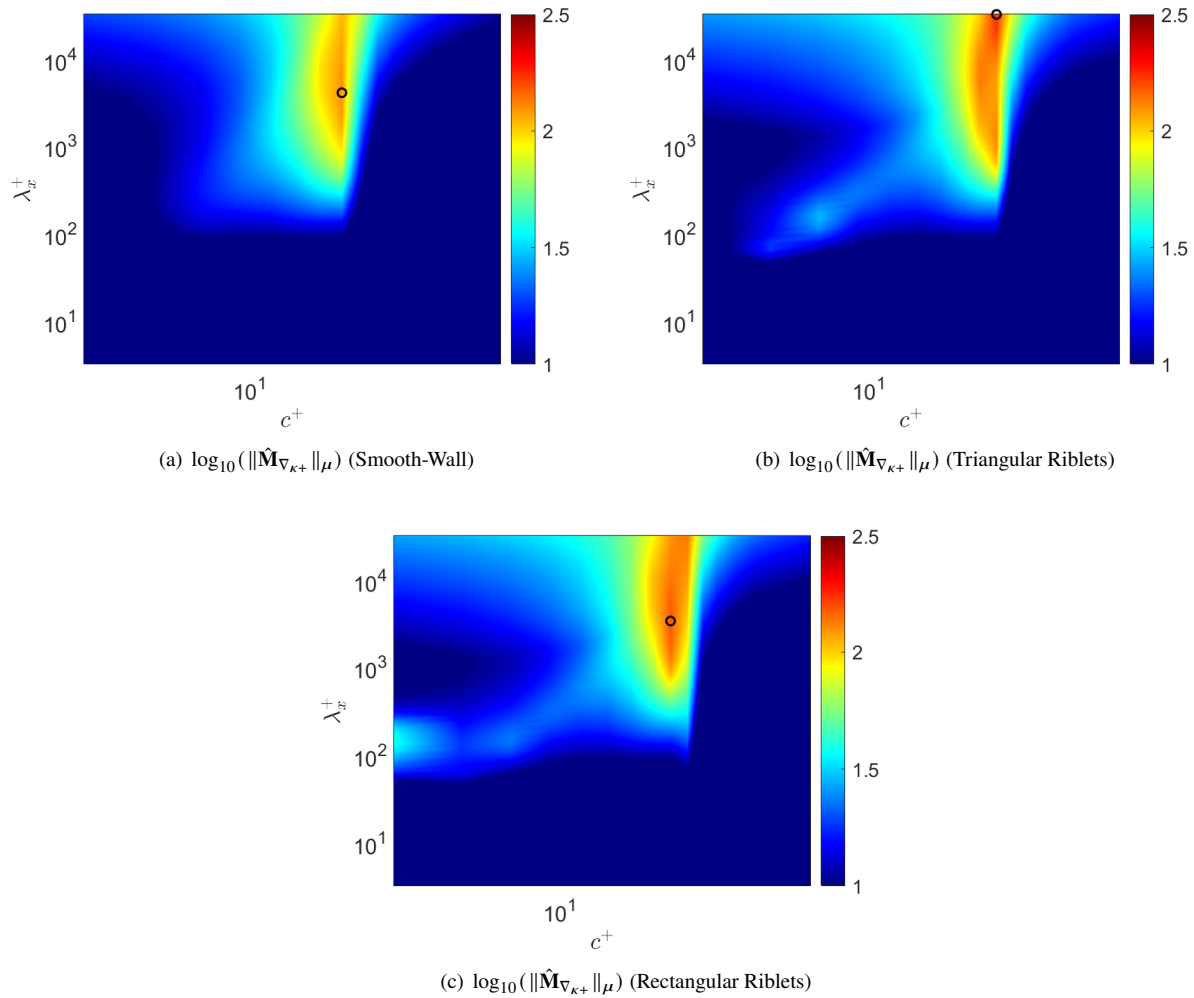
Fig. 6   The plots depict the singular values for c^+ vs λ_x^+. The black circle indicates the maximum value on the heat plot.
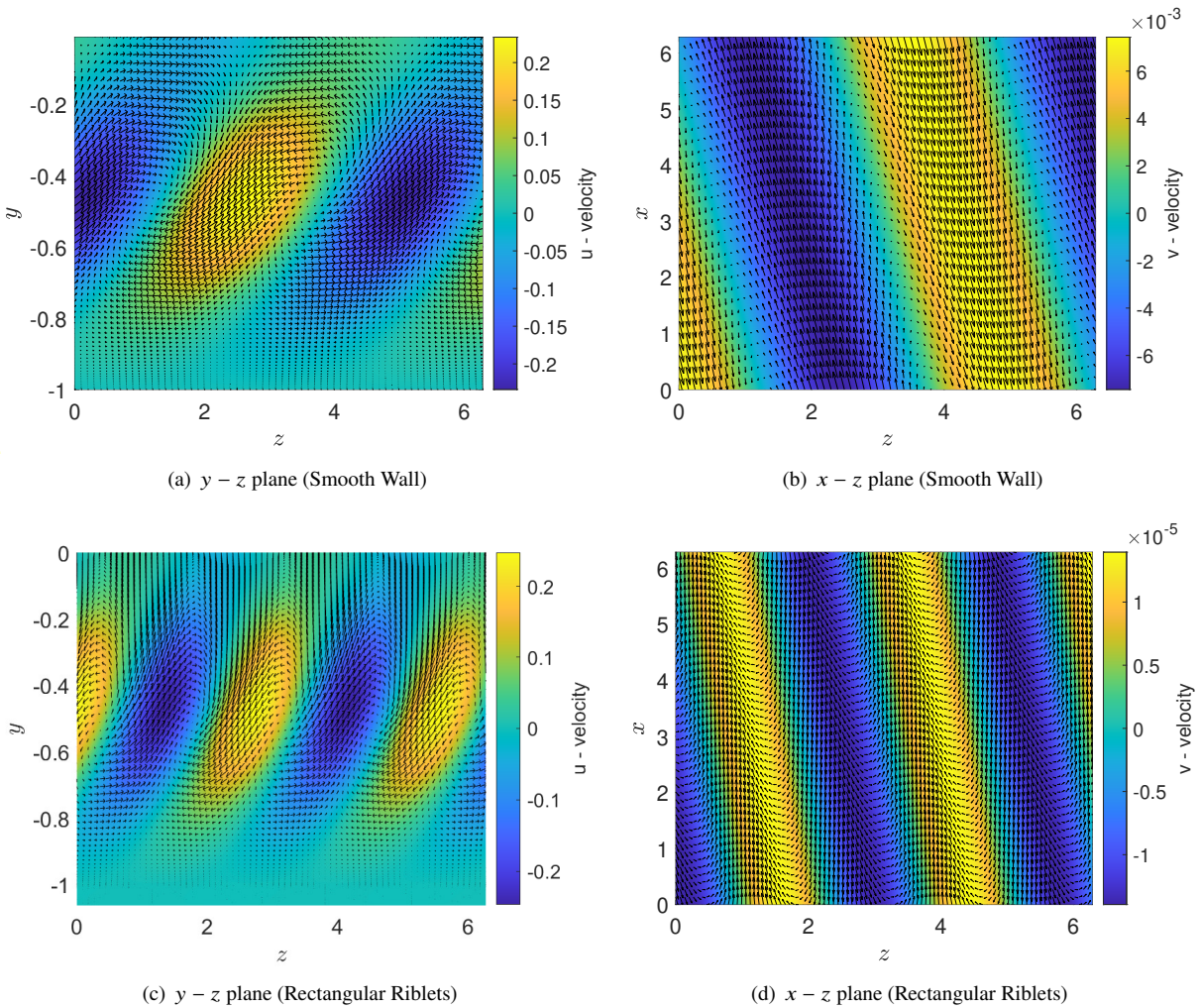
(a) $y - z$ plane (Smooth Wall)

(b) $x - z$ plane (Smooth Wall)

(c) $y - z$ plane (Rectangular Riblets)

(d) $x - z$ plane (Rectangular Riblets)

Fig. 7   (Top Left) The plot indicates a lift-up mechanism with rotations at the center of the flow domain. The contours are $u-$velocities and the vector field is $v - w$ velocities. (Top Right) A top-down view of the flow at $y \approx -0.5$. We can see that the structures are diagonally oriented. Contours indicate $v-$velocity and the vector field is the $u - w$ velocities. (Bottom Left) The plot indicates a lift-up mechanism with rotations at the center of the flow domain. The contours are $u-$velocities and the vector field is $v - w$ velocities. (Bottom Right) A top-down view of the flow at $y \approx -1$. We can see that the structures are diagonally oriented. Contours indicate $v-$velocity and the vector field is the $u - w$ velocities.

15
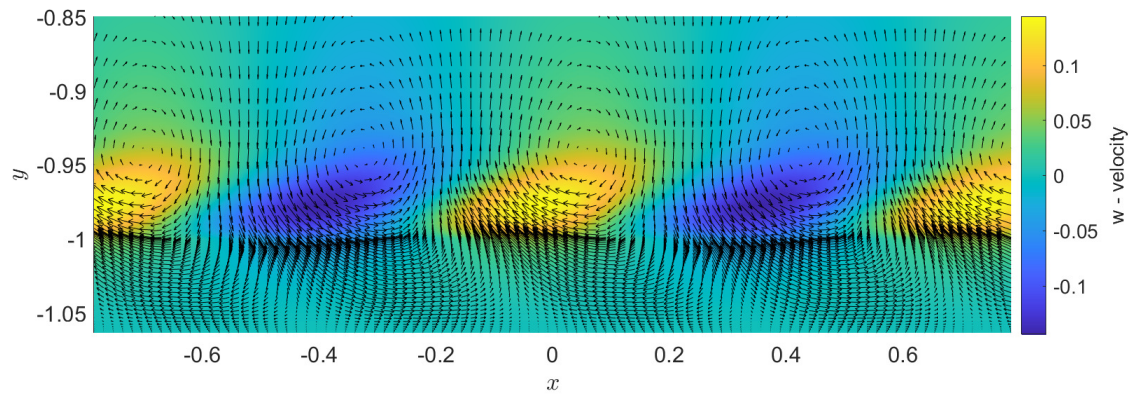
(a) Kelvin-Helmholtz Vortices (Power - Iteration)
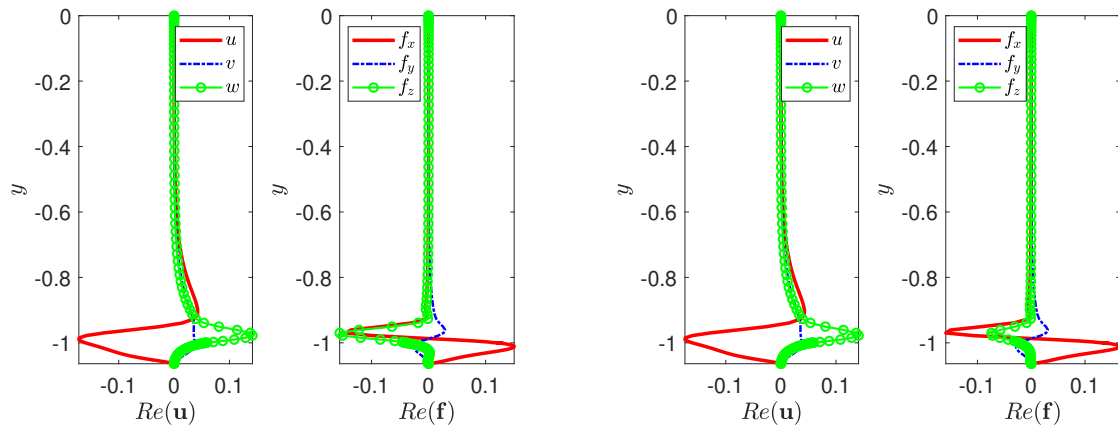
(b) Power-Iteration

(c) Resolvent SVD

Fig. 8 **The modes shapes indicated are associated with KH vortices at $\lambda_x^+ = 1.36 \times 10^2$, $\lambda_z^+ = 3.47 \times 10^2$ and $c^+ = 4$.**

V. Conclusion

We showed that imposing some structure of the nonlinearity in feedback with linear dynamics yields less conservative estimates of the I/O gains than the traditional resolvent analysis. In doing so, we were able to make deductions about the stabilizing effects of different riblet shapes using the I/O gain plots to study the largest gain values and modes highlighted. Additionally, the SSV approach allowed us to directly extract physically meaningful mechanisms that are not highlighted by the traditional resolvent methods such as NW-cycle and lift-up mechanism. The highlighted mechanisms not only are easily extracted using the SSV method but also are physically consistent with some of the insights obtained from the high-fidelity methods in the fluids literature. Given the usefulness of incorporating the structure of nonlinearity in the I/O analysis, it would be beneficial to exploit the true underlying Δ structure instead of the relaxed version used in this paper. Thus, in future works, we hope to use the repeated complex full-block Δ structure, which would allow us to improve the reduced-complexity approach to gain better insights into the underlying mechanisms responsible for flow instabilities.

VI. Acknowledgments

References

[1] Cousteix, J., "Aircraft Aerodynamic Boundary Layers," *Encyclopedia of Physical Science and Technology (Third Edition)*, edited by R. A. Meyers, Academic Press, New York, 2003, third edition ed., pp. 301–317.

[2] Jovanović, M. R., and Bamieh, B., "Componentwise energy amplification in channel flows," *Journal of Fluid Mechanics*, Vol. 534, 2005, pp. 145–183.

[3] Chavarin, A., and Luhar, M., "Resolvent analysis for turbulent channel flow with riblets," *AIAA Journal*, Vol. 58, No. 2, 2020, pp. 589–599.

[4] Ran, W., Zare, A., and Jovanović, M. R., "Model-based design of riblets for turbulent drag reduction," *Journal of Fluid Mechanics*, Vol. 906, 2021, p. A7.

[5] Towne, A., Rigas, G., Kamal, O., Pickering, E., and Colonius, T., "Efficient global resolvent analysis via the one-way Navier–Stokes equations," *Journal of Fluid Mechanics*, Vol. 948, 2022, p. A9.

[6] McKeon, B. J., and Sharma, A. S., "A critical-layer framework for turbulent pipe flow," *Journal of Fluid Mechanics*, Vol. 658, 2010, pp. 336–382.

[7] Moarref, R., Jovanović, M., Tropp, J., Sharma, A., and McKeon, B., "A low-order decomposition of turbulent channel flow via resolvent analysis and convex optimization," *Physics of Fluids*, Vol. 26, No. 5, 2014, p. 051701.

[8] Bae, H. J., Dawson, S. T., and McKeon, B. J., "Studying the effect of wall cooling in supersonic boundary layer flow using resolvent analysis," *AIAA Scitech 2020 Forum*, 2020, p. 0575.

[9] Taira, K., Brunton, S. L., Dawson, S. T., Rowley, C. W., Colonius, T., McKeon, B. J., Schmidt, O. T., Gordeyev, S., Theofilis, V., and Ukeiley, L. S., "Modal analysis of fluid flows: An overview," *Aiaa Journal*, Vol. 55, No. 12, 2017, pp. 4013–4041.

[10] Jovanović, M. R., "From bypass transition to flow control and data-driven turbulence modeling: an input–output viewpoint," *Annual Review of Fluid Mechanics*, Vol. 53, 2021, pp. 311–345.

[11] Dwivedi, A., Gs, S., Candler, G. V., Nichols, J. W., and Jovanovic, M., "Input-output analysis of shock boundary layer interaction," *2018 Fluid Dynamics Conference*, 2018, p. 3220.

[12] Luhar, M., Sharma, A. S., and McKeon, B. J., "Opposition control within the resolvent analysis framework," *Journal of Fluid Mechanics*, 2014.

[13] Chavarin, A., and Luhar, M., "Optimization of Riblet Geometry via the Resolvent Framework," *AIAA SCITECH 2022 Forum*, 2022, p. 1037.

[14] Garcia-Mayoral, R., and Jimenez, J., "Hydrodynamic stability and breakdown of the viscous regime over riblets," *Journal of Fluid Mechanics*, Vol. 678, 2011, pp. 317–347.

[15] Liu, C., and Gayme, D. F., "Input-output inspired method for permissible perturbation amplitude of transitional wall-bounded shear flows," *Phys. Rev. E*, Vol. 102, 2020, p. 063108.

[16] Kalur, A., Mushtaq, T., Seiler, P., and Hemati, M. S., "Estimating Regions of Attraction for Transitional Flows using Quadratic Constraints," *IEEE Control Systems Letters*, 2021, pp. 1–1.

[17] Kalur, A., Seiler, P., and Hemati, M. S., "Nonlinear stability analysis of transitional flows using quadratic constraints," *Physical Review Fluids*, Vol. 6, No. 4, 2021, p. 044401.

[18] Heins, P. H., Jones, B. L., and Sharma, A. S., "Passivity-based output-feedback control of turbulent channel flow," *Automatica*, 2016.

[19] Sharma, A. S., Morrison, J. F., McKeon, B. J., Limebeer, D. J. N. L., Koberg, W. H., and Sherwin, S. J., "Relaminarisation of $Re_\tau = 100$ channel flow with globally stabilising linear feedback control," *Physics of Fluids*, Vol. 23, No. 12, 2011, p. 125105.

[20] Liu, C., and Gayme, D. F., "Structured input–output analysis of transitional wall-bounded flows," *Journal of Fluid Mechanics*, Vol. 927, 2021.

[21] Mushtaq, T., Bhattacharjee, D., Seiler, P. J., and Hemati, M., "Structured Input-Output Tools for Modal Analysis of a Transitional Channel Flow," *AIAA SCITECH 2023 Forum*, 2023, p. 1805.

[22] Mushtaq, T., Bhattacharjee, D., Seiler, P., and Hemati, M. S., "Structured Singular Value of a Repeated Complex Full Block Uncertainty," *Submitted to International Journal of Robust and Nonlinear Control for Review*, 2023. https://doi.org/10.48550/arXiv.2211.05929.

[23] Bhattacharjee, D., Mushtaq, T., Seiler, P. J., and Hemati, M., "Structured Input-Output Analysis of Compressible Plane Couette Flow," *AIAA SCITECH 2023 Forum*, 2023, p. 1984.

[24] Doyle, J., "Analysis of feedback systems with structured uncertainties," *IEE Proceedings D-Control Theory and Applications*, Vol. 129, IET, 1982, pp. 242–250.

[25] Packard, A., and Doyle, J., "The complex structured singular value," *Automatica*, Vol. 29, No. 1, 1993, pp. 71–109.

[26] Safonov, M. G., "Stability margins of diagonally perturbed multivariable feedback systems," *IEE Proceedings D (Control Theory and Applications)*, Vol. 129, IET, 1982, pp. 251–256.

[27] Khadra, K., Angot, P., Parneix, S., and Caltagirone, J.-P., "Fictitious domain approach for numerical modelling of Navier–Stokes equations," *International journal for numerical methods in fluids*, Vol. 34, No. 8, 2000, pp. 651–684.

[28] Reynolds, W., and Tiederman, W., "Stability of turbulent channel flow, with application to Malkus's theory," *Journal of Fluid Mechanics*, Vol. 27, No. 2, 1967, pp. 253–272.

[29] Del Alamo, J. C., and Jiménez, J., "Spectra of the very large anisotropic scales in turbulent channels," *Physics of Fluids*, Vol. 15, No. 6, 2003, pp. L41–L44.

[30] Del Alamo, J. C., Jiménez, J., Zandonade, P., and Moser, R. D., "Scaling of the energy spectra of turbulent channels," *Journal of Fluid Mechanics*, Vol. 500, 2004, pp. 135–144.

[31] Aurentz, J. L., and Trefethen, L. N., "Block operators and spectral discretizations," *SIAM review*, Vol. 59, No. 2, 2017, pp. 423–446.

[32] Braatz, R., Young, P., Doyle, J., and Morari, M., "Computational Complexity of μ Calculation," *IEEE Trans. on Aut. Control*, Vol. 39, No. 5, 1994, pp. 1000–1002.

[33] Demmel, J., "The componentwise distance to the nearest singular matrix," *SIAM J. Matrix Anal. Appl.*, Vol. 13, No. 1, 1992, pp. 10–19.

[34] Troeng, O., "Five-Full-Block Structured Singular Values of Real Matrices Equal Their Upper Bounds," *IEEE Control Systems Letters*, Vol. 5, No. 2, 2021, pp. 583–586.

[35] Colombino, M., and Smith, R. S., "A Convex Characterization of Robust Stability for Positive and Positively Dominated Linear Systems," *IEEE Transactions on Automatic Control*, Vol. 61, No. 7, 2016, pp. 1965–1971.

[36] Zhou, K., Doyle, J., and Glover, K., *Robust and Optimal Control*, Prentice Hall, 1996.

[37] Boyd, S., and El Ghaoui, L., "Method of centers for minimizing generalized eigenvalues," *Linear algebra and its applications*, Vol. 188, 1993, pp. 63–111.

[38] Boyd, S., El Ghaoui, L., Feron, E., and Balakrishnan, V., *Linear matrix inequalities in system and control theory*, SIAM, 1994.

[39] Nesterov, Y. E., and Nemirovskii, A., "An interior-point method for generalized linear-fractional programming," *Mathematical Programming*, Vol. 69, No. 1, 1995, pp. 177–204.

[40] Osborne, E. E., "On Pre-Conditioning of Matrices," *J. ACM*, Vol. 7, No. 4, 1960, p. 338–345.

[41] Zhou, K., and Doyle, J. C., *Essentials of robust control*, Vol. 104, Prentice hall Upper Saddle River, NJ, 1998.

[42] Vreman, A., and Kuerten, J. G., "Comparison of direct numerical simulation databases of turbulent channel flow at Re τ= 180," *Physics of Fluids*, Vol. 26, No. 1, 2014, p. 015102.

[43] Endrikat, S., Modesti, D., García-Mayoral, R., Hutchins, N., and Chung, D., "Influence of riblet shapes on the occurrence of Kelvin–Helmholtz rollers," *Journal of Fluid Mechanics*, Vol. 913, 2021, p. A37.

Appendix

Here, we will provide details about the derivation of the reduced-order form of (4). We take the divergence of (4) and substitute the incompressibility constraint:

$$\nabla^2 p = -2U_b^y v^x - 2U_b^z w^x - \nabla \cdot \mathbf{f} - (K^{-1})^y v - (K^{-1})^z w. \tag{25}$$

Then, we take the Laplacian of the *y*-momentum equation in (4) and substitute the expression for $\nabla^2 p$, which will yield the wall-normal velocity equation:

$$\nabla^2 v^t = [\frac{1}{Re_\tau}\nabla^4 + U_b^{yy}\partial_x - U_b\nabla^2\partial_x - (K^{-1})^y\partial_y - U_b^{zz}\partial_x - 2U_b^z\partial_{xz} - 2(K^{-1})^z\partial_z - (K^{-1})^{zz} - K^{-1}\nabla^2]v$$
$$+ [2U_b^{yz}\partial_x + 2U_b^z\partial_{xy} + (K^{-1})^{yz} + (K^{-1})^z\partial_y]w - \nabla^2 f_y + \partial_y(\nabla \cdot \mathbf{f}). \tag{26}$$

Now, we take the curl of the momentum equations to obtain the wall-normal vorticity equation as the following:

$$\omega_y^t = [\frac{1}{Re_\tau}\nabla^2 - U_b\partial_x - K^{-1}]\omega_y - [U_b^z\partial_x + (K^{-1})^z]u - [U_b^y\partial_z + U_b^{yz}]v - [U_b^z\partial_z + U_b^{zz}]w - f_x^z + f_z^x \tag{27}$$

where ω_y is the wall-normal vorticity. Notice that (26) and (27) are coupled with *u* and *w* components of the velocity vector. To remove this coupling, we can simply form a transformation matrix **T** such that $\psi = \mathbf{T}\mathbf{u}$, where $\psi = \begin{bmatrix} v & \omega_y \end{bmatrix}^\mathrm{T}$. Hence, we have the following:

$$\begin{bmatrix} v \\ \omega_y \end{bmatrix} = \begin{bmatrix} 0 & 1 & 0 \\ \partial_z & 0 & -\partial_x \end{bmatrix} \begin{bmatrix} u \\ v \\ w \end{bmatrix} \tag{28}$$

We can add another row to the **T** matrix to make it invertible. One choice is to use $\nabla \cdot \mathbf{u} = 0$:

$$\begin{bmatrix} 0 \\ v \\ \omega_y \end{bmatrix} = \begin{bmatrix} \partial_x & \partial_y & \partial_z \\ 0 & 1 & 0 \\ \partial_z & 0 & -\partial_x \end{bmatrix} \begin{bmatrix} u \\ v \\ w \end{bmatrix} \tag{29}$$

We can simply invert the transformation matrix and use only the last two columns:

$$\mathbf{u} = \begin{bmatrix} -\partial_{xy} & \partial_z \\ (\partial_{xx} + \partial_{zz}) & 0 \\ -\partial_{yz} & -\partial_x \end{bmatrix} (\partial_{xx} + \partial_{zz})^{-1} \psi = \mathbf{T}^{-L}\psi \tag{30}$$

where $\mathbf{T}^{-L}$ is the left-inverse of $\mathbf{T}$. Finally, the dynamical equations will be the following:

$$\psi^t = \left(\begin{bmatrix} 0 & 0 \\ 0 & \frac{1}{Re_\tau}\nabla^2 - U_b\partial_x - K^{-1} \end{bmatrix} + \begin{bmatrix} 0 & A_{12} & A_{13} \\ A_{21} & A_{22} & A_{23} \end{bmatrix} \mathbf{T}^{-L} \right) \psi + \begin{bmatrix} \nabla^{-2}\partial_{xy} & \nabla^{-2}\left(\partial_{yy} - \nabla^2\right) & \nabla^{-2}\partial_{yz} \\ -\partial_z & 0 & \partial_x \end{bmatrix} \mathbf{f} \quad (31)$$

where,

$$A_{12} = \nabla^{-2}\left(\frac{1}{Re_\tau}\nabla^4 + U_b^{yy}\partial_x - U_b\nabla^2\partial_x - (K^{-1})^y\partial_y - U_b^{zz}\partial_x - 2U_b^z\partial_{xz} - 2(K^{-1})^z\partial_z - (K^{-1})^{zz} - K^{-1}\nabla^2 \right)$$

$$A_{13} = \nabla^{-2}\left(2U_b^{yz}\partial_x + 2U_b^z\partial_{xy} + (K^{-1})^{yz} + (K^{-1})^z\partial_y \right)$$

$$A_{21} = -U_b^z\partial_x - (K^{-1})^z$$

$$A_{22} = -U_b^y\partial_z - U_b^{yz}$$

$$A_{23} = -U_b^z\partial_z - U_b^{zz}$$

20